Particle & Particle Systems Characterization
www.particle-journal.com

One-Step Aerosol Synthesis of Thiocyanate Passivated Hybrid Perovskite Microcrystals: Impact of (Pseudo-)Halide Additives on Crystallization and Access to a Novel Binary Model

Ulrich J. Bahnmüller, Yaşar Krysiak, Tobias Seewald, Yenal Yalçinkaya, Denis Pluta, Lukas Schmidt-Mende, Stefan A. L. Weber, and Sebastian Polarz*

Hybrid Perovskite materials have gone through an astonishing development due to their unique optoelectronic behavior, leading to the creation of a wide range of synthetic strategies. As the materials' surface is found to play a crucial role with respect to the properties, e.g. hydration, stability and carrier mobilities, considerable efforts have been made to optimize the surface through various approaches. Especially the passivation of the perovskite surface attracted a lot of attention in this field, often resulting in more complex, multi-step synthetic processes. In this study, a simple one-step aerosol-assisted synthetic approach is presented to obtain thiocyanate (SCN) passivated single-crystal $MAPbBr_3$ microcrystals. To elucidate the role of the additive in the crystallization process, mixed (pseudo-)halide precursors are systematically investigated. The as processed, passivated microcrystals exhibit enhanced stability and charge carrier lifetimes. Additionally, a decrease in surface photovoltage, attributed to the presence of the SCN additive, is observed. Furthermore, the aerosol process is further developed resulting in a novel binary system containing $MAPbBr_3$-SCN perovskite microcrystals and Au nanostructures. This system serves as a promising model for further investigations into potential interactions between plasmonic and semiconducting materials, with initial results indicating prolonged charge carrier lifetimes.

1. Introduction

Hybrid perovskites have been one of the fastest-growing research topics over the past dozen years since their discovery as promising semiconductor materials.[1,2] Due to their unique optoelectronic properties combined with an easy and inexpensive synthesis and their structural flexibility,[3–5] they became of great interest for semiconductor applications.[6,7] A broad variety of different shapes such as films, nanoparticles, or macroscopic single crystals have been available to address the requirements of different applications. As a wide bandgap semiconductor, $MAPbBr_3$ perovskite materials have attracted great interest in the field of tandem or wide bandgap solar cells, light–emitting diodes (LEDs), and irradiance sensors.[8–10] In contrast to their convincing optoelectronic properties hybrid perovskite materials exhibit low stability to various environmental influences like humidity, irradiation, and heat,[11–14] which are key factors for their application as

U. J. Bahnmüller, Y. Krysiak, S. Polarz
Institute of Inorganic Chemistry
Leibniz University Hannover
Callinstrasse 9, 30167 Hannover, Germany
E-mail: ulrich.bahnmueller@aca.uni-hannover.de

The ORCID identification number(s) for the author(s) of this article can be found under https://doi.org/10.1002/ppsc.202400132

DOI: 10.1002/ppsc.202400132

T. Seewald, L. Schmidt-Mende
Department of Physics
University of Konstanz
Universitätsstrasse 10, 78457 Konstanz, Germany

Y. Yalçinkaya, S. A. L. Weber
Max-Planck-Institute for Polymeric Research
Ackermannweg 10, 55128 Mainz, Germany

D. Pluta
Institute of Physical Chemistry and Electrochemistry
Leibniz University Hannover
Callinstrasse 3A, 30167 Hannover, Germany

S. A. L. Weber
Institute for Photovoltaics
University of Stuttgart
Pfaffenwaldring 47, 70569 Stuttgart, Germany

semiconductors in the aforementioned fields, and much work has been done to increase the stability of these materials. However, Bakr et al. found that macroscopic single crystals (SC) are superior compared to the widely distributed polycrystalline films due to the absence of inhomogeneity and grains and their enhanced crystallinity.[15,16] They summarized the advantages of SC materials and the importance of controlling defects in an comprehensive review.[17] The surface of the macroscopic SCs was found to be crucial in terms of optoelectronic properties and stability.[18] Furthermore, Almadori et al. performed extensive investigations on the surface potential and the surface photovoltage of macroscopic $MAPbBr_3$ SCs.[19] They reported the relationship between the determined surface photovoltage (SPV) and the band bending of the material. Furthermore, the band bending is known to be influenced by the presence of defects in the surface region of the perovskite material.[20–22] To further improve the properties and stability of perovskite SCs by passivating the surface, post-synthesis treatments have been performed, often requiring additional synthesis steps.[23,24] An extensive review of various passivation methods was provided by Xia et al.[25] Different Lewis acids have been found to passivate the incomplete coordination of Pb, caused by X^- vacancies, by forming coordination or even covalent bonds. With respect to polycrystalline materials, pseudohalide species have attracted much interest in this field, especially the thiocyanate (SCN) anion. Extensive reviews have reported about improvements in the field of polycrystalline materials, e.g. increased stability and improved optoelectronic properties by increasing grain size and passivating grain boundaries.[26,27] To the best of our knowledge there have been no reports combining SCN additives and hybrid perovskite SC materials.

Due to the broad variety of different material shapes and compositions and the high interest in hybrid perovskite materials, a wide range of synthetic approaches has been developed and established.[28,29] Anti-solvent and inverse temperature crystallization (ITC) have become the most important approaches due to the ease of synthesis with respect to SC materials.[15,30] In particular, the ITC method has attracted a lot of interest attributed to its fast growth rate and a wide range of adaptations in the field of SC perovskite synthesis.[16,31] By utilizing a liquid single-source precursor (SSP) that contains all components of the desired product, and its conversion via ITC into the desired hybrid perovskite crystals, it was found that the retrograde solubility of $MAPbBr_3$ in *N,N*-dimethylformamide (DMF) and $MAPbI_3$ in γ-butyrolactone, are suitable systems.[31] Our group invented a glycol-based SSP system that provides access to tailored hybrid perovskite materials through various anti-solvent and inverse temperature approaches.[32–36] This SSP was adapted to yield SC $MAPbBr_3$ microcrystals from an ITC-based, aerosol-assisted synthetic approach.[37] In a subsequent study we were able to further optimize the SSP and aerosol setup resulting in a ligand-free synthesis of microcrystals with defined and facet-selective surfaces,[38] which were used to create a model system for studies of shape-property relationships of $MAPbBr_3$ perovskites. Furthermore, in our recent work, we have extended this model system to understand how kinetic aspects can influence the stability of these materials.[39] It was shown, that a small change in the crystallographic system, either by the change of the crystal direction or by using only a small amount of substituent, can improve the stability of the rather unstable material, without significantly affecting the optoelectronic properties.

In this work, we extend our SSP system to obtain a SCN passivation of $MAPbBr_3$ SC microcrystals by a simple one-step ITC approach. To gain insight into the crystallization kinetics being influenced by the additives, time-dependent UV–vis measurements were performed. The microcrystals obtained from the aerosol-assisted approach are perfect candidates to characterize the final product, without any structural changes, such as grain size for polycrystalline materials, which mechanically influence the properties.[40] In addition, they were found to be amplifiers with respect to these investigations due to their increased surface area compared to macroscopic SCs.[39] Furthermore, the microcrystals are free from size dependent effects, as they are present in nanoparticle systems.[41,42] In order to identify the influence on the properties of the SC microcrystals, the surface dependent properties have been investigated, e.g. by determining the SPV value for individual crystal facets of a single microcrystal. Finally, the pseudohalide passivated microcrystals were used to create a binary material, by combining them with plasmonic gold NPs immobilized by a second aerosol process. In this field, theoretical investigations have been reported on a similar binary material, Au nanoparticles incorporated into $MAPbI_3$ perovskite films, to potentially enhance the absorption by plasmonic near-field and scattering effects.[43] To date, synthetic approaches for the investigation and development of these binary materials are scarcely reported for hybrid perovskite materials.[44,45] The presented aerosol process offers a straightforward approach to combine both materials without the use of solvents causing degradation of the hybrid perovskite material,[46] thereby making the binary model readily accessible for further investigations.

2. Results and Discussion

2.1. The role of Anionic Additives in the Crystallization of $MAPbBr_3$ Microcrystals

In this work we aim to demonstrate the compositional flexibility of the liquid SSP system and take advantage of the aerosol-assisted synthesis to obtain SCN-passivated SC $MAPbBr_3$ microcrystals from a simple one-step ITC approach. Since mixed halides are well known in the case of hybrid perovskite materials,[47–49] they are the perfect candidates to demonstrate the flexibility of the SSP system with respect to anionic additives and to investigate their influence on the crystallization process. Therefore, different ratios of MACl and MAI were added to the SSP. The successful synthesis of the desired perovskite material on the micrometer scale can be seen from the SEM images (Figure S1, Supporting Information). The presence of the cubic $MAPbBr_3$ perovskite crystal structure and the phase purity of all samples discussed in this chapter are proven by the corresponding PXRD pattern (Figure S2, Supporting Information).[50] This confirms the successful crystallization of perovskite microcrystals for all compositions of SSPs. The enlargement of the PXRD pattern shows a slight shift of the reflexes toward larger and smaller angles for the microcrystals obtained from MACl and MAI containing SSPs (Figure S3, Supporting Information). In the case of MACl the shift toward larger angles and conversely toward smaller angles for MAI can be explained by the slight

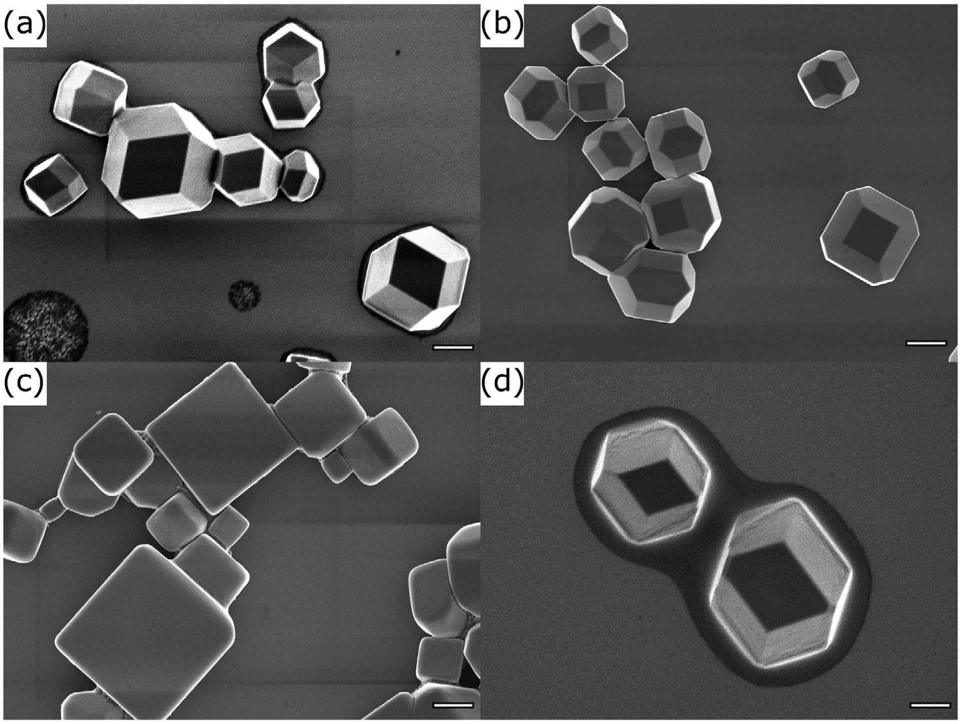

Figure 1. SEM images of microcrystals obtained from using SSPs with an excess of a) 0.1 eq MAI, b) 0.1 and c) 0.3 eq MACl and d) with 0.1 eq MACl and the initial amount of MABr reduced to 0.9 eq related to PbBr2; scale bars = 1000 nm.

shrinkage and expansion of the unit cell caused by the substitution of the Br anion by the corresponding smaller and larger homolog.[48,49] Since mixed halides are well known to tune the bandgap energy of hybrid halide perovskites, the bandgap energies of the different mixed halide materials were determined from the Tauc plots (Figure S4, Supporting Information). The absolute values are presented in Figure S4a (Supporting Information) and show the expected blue shift in case of MACl depending on the amount of additive used, or an energetic red shift for MAI. For comparison, the corresponding UV–vis absorbance spectra for the mixed halide materials are shown in Figure S5 (Supporting Information). The presence of iodide in the obtained microcrystals was further confirmed by EDX spectroscopy, which revealed the specific L_{α} line at 3.95 keV (Figure S6, Supporting Information). Thus, the successful incorporation of $Cl^{-}$and I^{-}, after the substitution of the A cation was already demonstrated in a previous work,[39] further underlines the flexibility of the SSP and the aerosol process toward anionic additives. Interestingly, the presence of different halide additives not only tunes the optoelectronic properties and crystal lattice but also affects the crystallization process, resulting in morphological changes. Previous reports indicate that adding larger amounts of MABr to the SSP alters the morphology of the resulting microcrystals.[38] This phenomenon is attributed to the increased activity of Pb species with higher MABr ratios, which promotes the formation of the thermodynamically favored (001) facet. Depending on the excess MABr amount, rhombododecahedral (RD), edge-cut cubic (ECC), or cubic (CU) morphologies are obtained. A schematic illustrating the transition from (011)-terminated RD to mixed (011) and (001)-terminated ECC to (001)-terminated CU is shown in Figure S7 (Supporting Information). The morphological changes induced by mixed halide additives are evident from the SEM images in **Figure 1**. Using 0.1 eq MAI as an additive result in RD-shaped microcrystals (Figure 1a), while the same amount of MACl (Figure 1b) produces ECC morphology, and further increasing the MACl amount yields CU shapes (Figure 1c). When the initial MABr amount is reduced to 0.9 eq relative to PbBr2 and 0.1 eq MACl is added to achieve an equimolar MAX:$PbBr_2$ ratio RD microcrystals were obtained again (Figure 1d). This trend is further confirmed when the pseudo-halide species MASCN was used as additive. The SEM images of the microcrystals obtained from the series of MASCN-containing SSPs are presented in **Figure 2**. Since SCN^{-} is not expected to be incorporated into the crystal lattice, the characterization of the resulting materials is discussed in detail in the following section. For comparison, RD microcrystals obtained from an equimolar ratio SPP with respect to MABr:$PbBr_2$ are shown in Figure 2a. As the MASCN to $PbBr_2$ ratio increases from 0.1 (Figure 2b), to 0.8 (Figure 2c) and to 1.2 eq (Figure 2d) the morphologies transition from RD, over ECC to CU, respectively. As the transition of morphologies is fluid with mixed facet termination, the size and the ratio of different facets, i.e., the crystal habit, can vary slightly due to minimal changes in the activity of the lead species within the SSP (Figure S7, Supporting Information).[38] Since larger amounts of MASCN are required to alter the morphology, an intermediate morphology was investigated. The 0.4 eq SSP resulted in an intermediate state between RD and ECC shaped microcrystals (Figure S8a, Supporting Information). As a result, a clear differentiation between the morphologies is difficult in this case since the intermediate shaped microcrystals appear to be whether RD

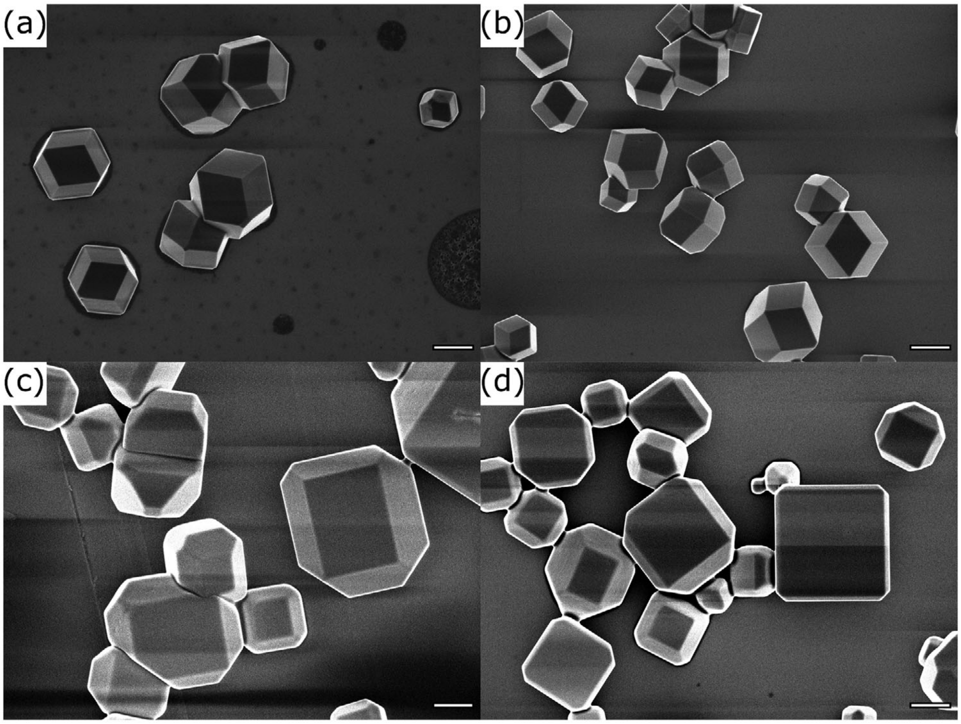

Figure 2. SEM images of a) $MAPbBr_3$ reference material; and synthesized with b) 0.1 eq, c) 0.8 eq, and d) 1.2 eq. MASCN additive; scalebars = 1 µm.

or ECC due to their different orientations. These different orientations on the substrate become possible according to the increasing presence of the (001) facet, i.e., the possibility to attach to the surface of the substrate by this new grown facet, which was not present for the initial RD morphology. To quantify the morphological behavior, the RD-like and ECC-like microcrystals related to their orientation were counted (Figure S8b, Supporting Information), resulting in an equal ratio of shapes. In addition, the morphology as a function of the amount and type of anionic additive was visualized in **Figure 3a**. Considering the results mentioned above regarding the SSP MABr ratio and the findings presented here, it is concluded that both the quantity and the anionic species of the additive influence the morphology of the obtained microcrystals. This phenomenon can be explained by the variation in bonding energy between Pb and the (pseudo-)halide additive, which affects the activity of the lead species within the SSP.[51,52]

To further support these findings kinetic measurements of the ITC of the SSPs were performed, as a correlation between kinetics and thermodynamics has been previously found.[38] Therefore, the crystallization process was investigated by time-dependent UV–vis measurements at a slightly elevated

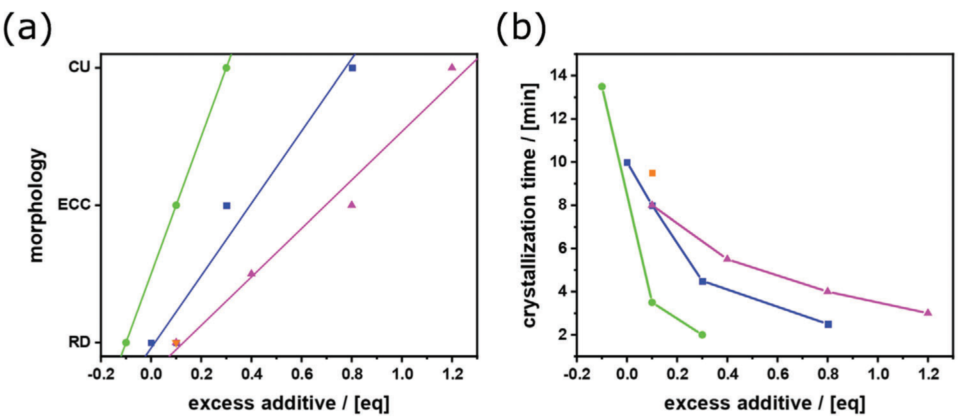

Figure 3. a) morphology dependency on the used amounts of the corresponding additives MACl (green circles), MABr (blue squares), MAI (orange triangle), and MASCN (magenta triangle); b) Crystallization times determined from UV–vis kinetic measurements, versus the amount of additive (same coloration as for a);values for 0.0 and 0.8 eq included from ref. [38] for clarification). For −0.1 eq MACl, the MABr amount was lowered to 0.9 eq regarding PbBr2, and 0.1 eq MACl was added.

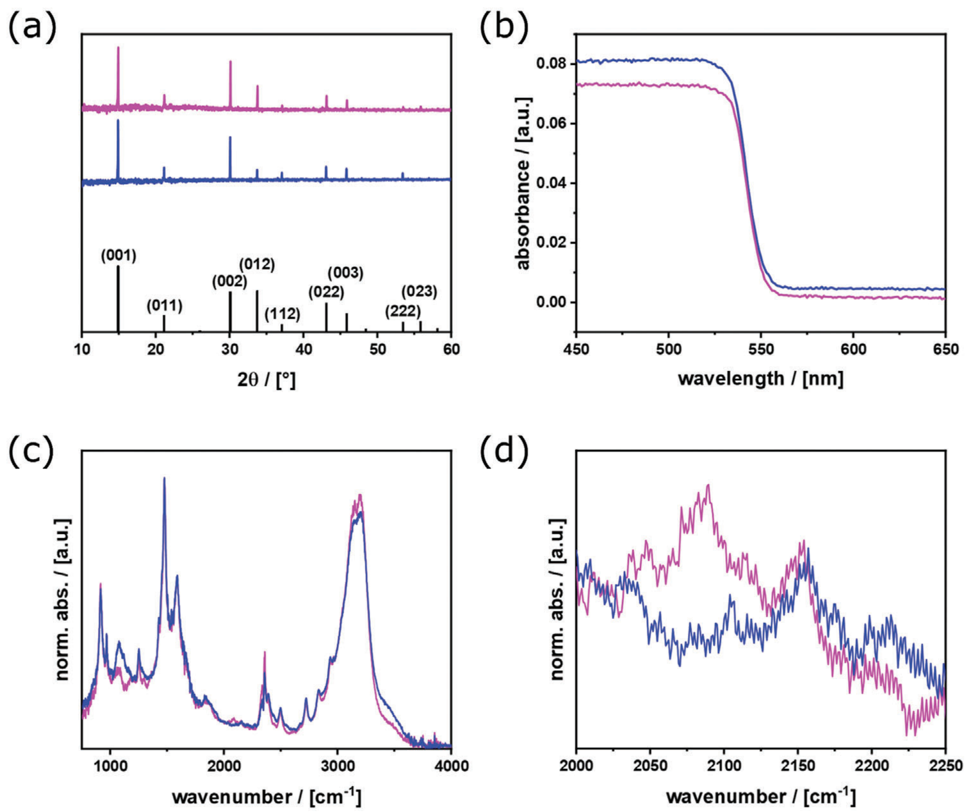

Figure 4. a) XRD pattern, b) UV–vis absorbance spectra and c) norm. IR spectra and d) zoom-in IR spectra of $MAPbBr_3$ reference (blue) and $MAPbBr_3$-SCN material (magenta); XRD reference pattern MAPbBr3 (black, No. 252 415.cif).

temperature of 75 °C to visualize the SSP to perovskite ITC. These measurements allow a direct statement on the kinetic influences of the additives on the crystallization of the perovskite microcrystals from the SSP. The determined crystallization times are shown in Figure 3b as a function of the additive equivalent used. It can be seen that increasing the amount of (pseudo-)halide added to the SSP generally results in an accelerated crystallization for all species investigated. The corresponding time-dependent measurements are shown in Figures S9–S18 (Supporting Information). The kinetic measurements clearly show that the crystallization time depends not only on the amount of halide used, but also on the anionic species present in the SSP. With 0.3 eq MACl, the crystallization time is less than halved compared to the more than doubled amount of 0.8 eq MABr. Furthermore, the addition of 0.1 eq MAI has almost no effect on the crystallization time, but the same amount of MACl causes a significant acceleration, reducing the crystallization time to about one-third compared to the additive-free reference. When the initial amount of MABr is reduced to 0.9 eq and 0.1 eq MACl is used to obtain a total MAX:$PbBr_2$ ratio of 1:1, the crystallization time is reduced. Similar results were reported by Yang et al. for the formation of $MAPbI_3$ films, when HI and HCl were added during the crystallization process to accelerate the film formation.[53] For the MASCN series, the crystallization process is also accelerated but larger amounts of additive are required, as expected from thermodynamic influences mentioned above.

Since the average particle sizes for the microcrystals obtained from the different SSPs are all in the same size range, they are perfect candidates to identify how SCN^- chemically affects the material properties and where it is located in the obtained microcrystals, without considering structural changes or size dependent effects, as known for polycrystalline films or nanoparticles.[40,42,54] The size ranges from several hundred nanometers up to a few micrometers, as can be seen from the survey SEM images (Figure S19, Supporting Information). The average particle size was found to be between 1.3 ± 0.4 and 1.6 ± 0.6 µm. These results are in agreement with previous reports, which have furthermore shown that there are no size-dependent changes in the optoelectronic properties.[38] An overview of the exact values is given in Figure S20 (Supporting Information). In the following section, the discussion will focus on the RD microcrystals obtained from the precursor containing 0.1 eq MASCN, to exclude any morphological or structural changes affecting the perovskite material properties.[40]

2.2. $MAPbBr_3$-SCN Perovskites Properties

The comparison of the XRD patterns of the 0.1 eq MASCN additive and the pure $MAPbBr_3$ reference system, hereafter referred to as $MAPbBr_3$-SCN and reference, is shown in **Figure 4**a. As mentioned above, both materials show the same reflexes, confirming the phase purity and the presence of the cubic $MAPbBr_3$

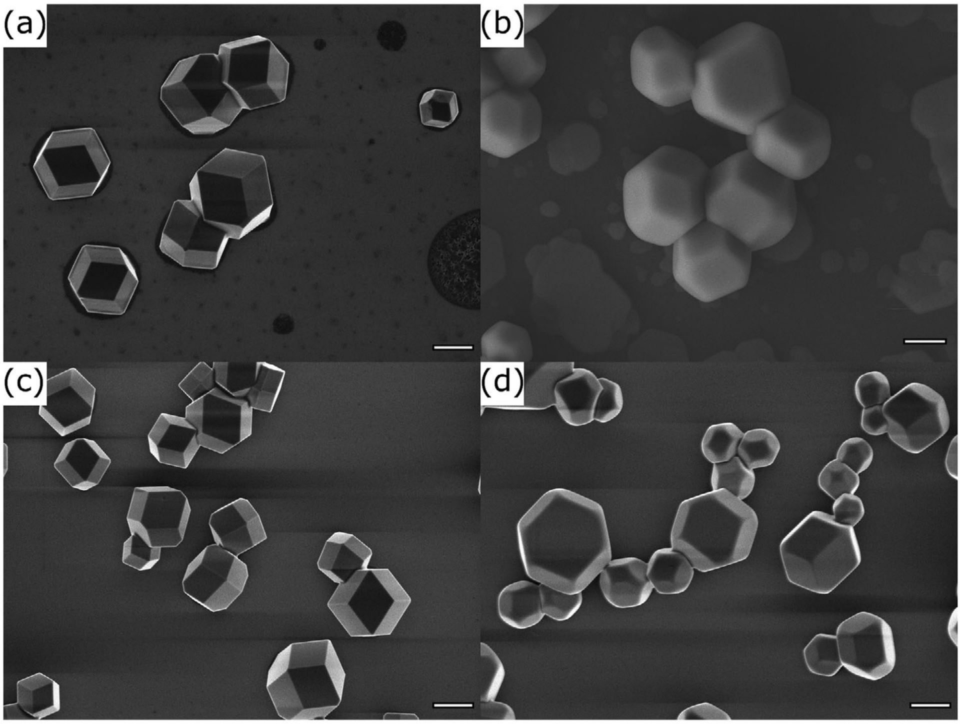

Figure 5. SEM images of $MAPbBr_3$ reference as prepared and b) stored under 53.1% rel. humidity for 72 h; c) MAPbBr3-SCN microcrystals as prepared and d) stored under 53.1% rel. humidity for 72 h; scalebars = 1 µm.

perovskite structure.[50] No shift of reflexes, as discussed above in the case of mixed halides, can be seen from the obtained pattern, suggesting that the larger SCN^- is not incorporated into the crystalline material in significant amounts during the aerosol process. This is consistent with a previous report by Cai et al. using SCN^- as additional ligand in the preparation of $MAPbBr_3$ NPs.[55] Additionally, the SC character of the obtained $MAPbBr_3$-SCN microcrystals was demonstrated by 3D ED measurements. The reconstructed crystallographic sections and modeled structures are shown in Figure S21 (Supporting Information). This proves that the SC character is still present and not affected by the presence of MASCN during the crystallization or within the surface of the finally obtained $MAPbBr_3$-SCN microcrystals. The UV–vis absorbance spectra, shown in Figure 4b, and thus the bandgap energy of $MAPbBr_3$-SCN, determined from the Tauc plot (Figure S22, Supporting Information), show no changes, compared to the reference (Figure S4, Supporting Information), yielding a bandgap energy of 2.27 eV. The IR spectra (Figure 4c) show the major shifts of prominent peaks of $MAPbBr_3$. The peaks at 970, 1480, 1590, and 3160 cm^{-1} can be assigned to C-N stretching, *sym*-NH_3^+ bending, *asym*-NH_3^+ bending and *sym*-NH_3^+ stretching, respectively.[56] From the zoomed-in IR spectra (Figure 4d) an additional absorbance band can be found at 2080 cm^{-1} for the $MAPbBr_3$-SCN microcrystals. The additional band is related to the C-N stretching vibration of the SCN.[40,57] For comparison, the IR spectrum of pure MASCN is shown in Figure S23a (Supporting Information) and reveals a slightly red-shifted stretching vibration at 2040 cm^{-1}. This energetic shift supports a change in the bonding situation of SCN^- due to the coordination on the perovskite surface and thus the presence of a passivation layer.[58] The higher energy for the stretching band can therefore be seen as indication for the coordination via the nitrogen atom and a triple bond between carbon and nitrogen (Figure S23b, Supporting Information). The results are consistent with an extensive theoretical study by Wang et al. which suggests the single coordination through the N atom to be preferred for hybrid perovskite materials.[59] Furthermore, since the IR spectra are measured in reflection mode and the penetration depth of the irradiation is known to be rather low, the SCN anions must be present on the surface of the obtained microcrystals and not affect the crystal system itself as previously demonstrated by the XRD pattern. Since it has already been confirmed that SCN^- can substitute the coordinating ligands in the dynamic system of perovskite nanoparticle dispersions,[55] it seems that a passivation layer is formed for the solid, rigid microcrystal system. If this is the case for $MAPbBr_3$-SCN, the surface related properties of the microcrystals have to change.

In order to clarify this assumption, further investigations regarding surface dependent properties were performed. The microcrystals were found to amplify the effects of physical and chemical triggers by morphological degradation before being detectable by composition dependent methods, e.g. PXRD.[39] Therefore, stability tests were performed by storing the microcrystals of $MAPbBr_3$-SCN and the reference $MAPbBr_3$ under the same conditions, applying a defined atmosphere with 53% relative humidity. When the samples are stored under these conditions, the $MAPbBr_3$-SCN microcrystals show higher morphological stability compared to the reference (**Figure 5**). As can be seen from the SEM images, the reference material shows quite strong rounding of the corners and edges (Figure 5b), while

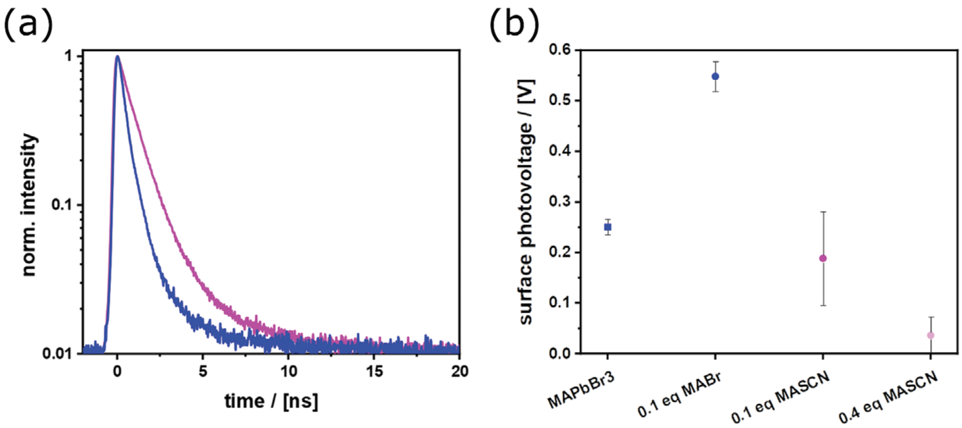

Figure 6. a) PL lifetime measurements of $MAPbBr_3$ (blue) and $MAPbBr_3$-SCN hybrid perovskite (magenta); and b) SPV values determined from KPFM measurements of samples prepared with and without MABr and MASCN additive.

the $MAPbBr_3$-SCN microcrystals (Figure 5d) remain almost untouched. Furthermore, the particle size does not change significantly after treating the microcrystals with humid air (Figure S20, Supporting Information). The microcrystal system allows the increasing stability to be directly related to the presence of thiocyanate in the perovskite material. In the case of polycrystalline materials structural reasons, such as increasing grain size, have been reported to cause the increased stability with SCN additives.[40,54] Since the size for the microcrystals reported is unchanged, the increased stability is directly related to the formation of a SCN surface layer, which chemically stabilizes the perovskite microcrystal by the associated encapsulation. To the best of our knowledge a chemical stabilization has only been reported for 2D $MA_2Pb(SCN)_2I_2$ layered structures, where the SCN is incorporated into and causes the 2D perovskite network.[60] With respect to 2D perovskite structures, the molecular species causing the reduced dimensionality automatically serves as passivator, stabilizing the enhanced surface. Therefore, the herein-reported results suggest the presence of SCN^- in the surface of the microcrystals, forming a passivation layer and preventing the microcrystals from hydration. Since a passivation layer will not only affect the stability of the hybrid perovskite microcrystals, but also affects the optoelectronic properties,[18] further investigations were carried out.

To further prove the presence of SCN in the surface of the microcrystals, the contact potential difference (CPD) was determined for both materials. Since the CPD is directly dependent on the surface of the sample, a passivation layer that chemically alters the surface, should result in an energetic shift. Similar changes have been demonstrated for various metal oxides and sulfides.[61,62] The CPD maps, shown in Figure S24 (Supporting Information) show a shift to a higher value of 0.17 ± 0.01 V for $MAPbBr_3$-SCN microcrystals compared to 0.06 ± 0.01 V for the $MAPbBr_3$ reference, relative to the FTO support. The relative change of the CPD can be directly related to the chemical change of the surface, i.e. to the presence of a passivation layer formed by SCN^-. As can be seen from the optoelectronic measurements, shown in **Figure 6**, there are significant changes in the optical properties of the obtained materials, whether MASCN was used or not. The determination of the charge carrier lifetimes by PL measurements, shown in Figure 6a, confirms a longer lifetime in the case of the $MAPbBr_3$-SCN material, compared to the reference. The absolute values for the lifetimes were obtained by a mono-exponential fit of the decay curves (Figure S25, Supporting Information). The charge carrier lifetime for the $MAPbBr_3$-SCN microcrystals is almost doubled to 1.12(2) ns compared to the reference, which was determined to be 0.60(5) ns. The extended lifetime is indicative for a lower number of surface defects present, which are known to act as recombination sites for charge carriers in hybrid perovskite materials, causing non-radiative recombination and thus reducing carrier lifetimes.[63] To further characterize the electronic properties of the microcrystals, the SPV was determined from KPFM measurements performed under irradiation. These measurements allow to directly study how a single microcrystal or even a single facet is affected by the SCN passivation. The SPV values presented in Figure 6b show a slight decrease for the obtained microcrystals when 0.1 eq MASCN is present during the crystallization, while the addition of the same excess MABr results in a strong increase. As already mentioned, the SPV can be related to the band bending, and thus correlated with the defect density of the material, especially with respect to its surface.[20,21] Therefore, the presented results emphasize that the number of surface defects present in the final material is reduced by the presence of SCN^-, passivating the surface of the microcrystals, i.e., reducing defective states by their coordination.[25] When additionally examining the (001) facet, present in the ECC morphology, it is found that the SPV is further significantly reduced. Since the (001) has already been demonstrated to provide a lower amount of surface defects compared to the (011) facet in a previous work,[38] this confirms the aforementioned trend in the correlation between the number of surface defects and the SPV value.

Both results, PL lifetime and SPV values, suggest that the presence of MASCN during the crystallization leads to a less defective crystalline material, as structural and size-dependent effects can be ruled out. Furthermore, the microcrystals obtained show superior stability against humidity. This can be explained by the passivation of the surface by SCN, which leads to a reduced number of surface defects. Thus, the addition of MASCN to the liquid SSP not only leads to surface passivation, but also seems to improve the crystal quality of the obtained microcrystals. Therefore, the MASCN additive addresses two important issues regarding hybrid perovskite applications: improved stability and enhanced optoelectronic properties. However, the results presented herein lead to the conclusion that the addition of MASCN can also provide an improvement for macroscopic $MAPbBr_3$ SCs being crystallized by a one-step ITC approach. Since the aerosol-assisted conversion follows the ITC approach, the results reported can be transferred to the commonly used ITC procedures to obtain larger-scale hybrid perovskite materials for further optimization. This is a promising finding with respect to the use of $MAPbBr_3$ perovskites as wide bandgap semiconductors, e.g. as absorbers in large bandgap solar cells, irradiance sensors, or LEDs.[8–10] Finally, the enhanced stability and the presence of a SCN passivation layer offers the possibility to further extend the model system by additional modification of the microcrystal surface. In the following section, we present the synthesis of this model system, by combining $MAPbBr_3$-SCN microcrystals and plasmonic Au NPs.

2.3. Au NPs Binary System

The post-synthetic combination of hybrid perovskite materials and Au nanostructures requires a mixing step of both materials. To demonstrate the importance of Au being present in a nanostructured form, PL measurements of the pure $MAPbBr_3$-SCN and Au sputtered materials are shown in Figure S26 (Supporting Information). The qualitative PL spectra of the $MAPbBr_3$-SCN microcrystals, show an intense emission signal at 540 nm, which is in agreement with previous reports for $MAPbBr_3$ microcrystals.[37,38] As can be seen from the spectra, the emission of the materials is almost and completely quenched when Au is sputtered on the perovskite surface, resulting in an almost complete or complete coating of the microcrystals, which can be seen from the corresponding SEM images (Figure S27, Supporting Information). To clarify that the strongly reduced emission is related to a quenching process and not to a lack of excitation due to a shielding by the Au layer, the Tauc plots, determined from UV–vis absorbance spectra, for Au sputtered $MAPbBr_3$-SCN materials are shown in Figure S28 (Supporting Information). It can be seen that the semiconductor is still optically active and accessible to excitation, and the bandgap energy is determined to be 2.27 eV and therefore not affected by the coating. However, the presence of an Au film is not suitable for improving the optoelectronic properties. Using a wet chemical approach makes larger amounts of solvent, which causes problems with solvation and recrystallization processes of the hybrid perovskite crystals.[46] An aerosol process offers an approach to combine the $MAPbBr_3$-SCN microcrystals with Au nanostructures using only small amounts of solvent, dispersing only one of the components. Furthermore, the amount of solvent reaching the perovskite microcrystals is further reduced by partial evaporation and condensation by applying a heating step. The substrates containing $MAPbBr_3$-SCN microcrystals were placed behind the tube furnace and an aerosol generated from the Au nanoparticle dispersion was carried through the setup by a nitrogen flow. The exact procedure is described in the experimental section. This process results in the immobilization of Au NPs on hybrid perovskite microcrystals, as shown in the SEM image of Figure S29a (Supporting Information). The EDX spectrum obtained from the binary system is shown in **Figure 7a** and reveals the presence of Au. The corresponding SEM image of the area examined by EDX, visualizing the presence of the nanostructures on the perovskite surface, is shown in Figure 7b. This demonstrates the presence of Au nanostructures and the successful combination of the two materials. Overall the perovskite $MAPbBr_3$-SCN microcrystals show sharp edges and a defined morphology with flat and smooth surfaces, as shown in the survey SEM image (Figure S29b, Supporting Information), which is important since the surface is known to be crucial for the semiconductor properties.[18] Comparing the SEM images (Figure S29b,c, Supporting Information) of the $MAPbBr_3$-SCN and $MAPbBr_3$ microcrystals processed with the Au NPs aerosol, it can be seen that the increased stability against humidity, mentioned in the previous section, plays a crucial role for the immobilization step. While the $MAPbBr_3$ reference material shows a significant roughening of the surface of the microcrystals, the $MAPbBr_3$-SCN ones remain almost untouched and still offer a flat surface. Therefore, the focus for the binary system was placed on the $MAPbBr_3$-SCN microcrystals in the following discussion.

The $MAPbBr_3$-SCN binary material was further characterized by analyzing its crystal system, which still shows the pure perovskite phase, as can be seen from the XRD pattern (Figure S30, Supporting Information). No phases from degradational products, such as lead halides or mixed oxides and hydroxides can be found.[13] The absence of Au-related reflexes can be explained by the comparatively small amount and size of Au NPs compared to the microcrystals, resulting in broad reflexes with low intensities. Since spherical Au NPs provide plasmon resonance at wavelengths similar to the bandgap energy of $MAPbBr_3$ they are difficult to be distinguished. Anisotropic nanorods (NRs) offer optical activity of two different wavelengths by longitudinal and transverse plasmons.[64] To obtain NRs in the binary system, the temperature of the immobilization step was modified, to prevent the nanorods from melting and thus resulting in spherical particles.[65] To achieve this goal, the temperature was lowered, resulting in the successful deposition of NRs as shown in the SEM image (Figure 7c). This shows that the aerosol approach offers the possibility to transfer even more sensitive anisotropic Au nanostructures without causing a loss of anisotropy, which prevents their unique optical properties.

In order to gain first insights into the optoelectronic behavior of the novel binary model system, PL spectra and lifetimes were determined and plotted in **Figure 8**. As mentioned in the previous section, the $MAPbBr_3$-SCN microcrystals are superior compared to their $MAPbBr_3$ references. The qualitative spectra shown in Figure 8a confirm this trend. After conversion to the binary Au functionalized system, the effect becomes even more pronounced when containing spherical Au NPs or anisotropic NRs. The values are shown in Figure 8b, for comparison of the binary materials and the pure perovskite reference. Charge carrier lifetimes of 1.15(5) and 1.35(0) ns are determined for the binary system containing Au NPs or NRs, respectively (Figure S31, Supporting Information). Compared to the lifetimes in the previous section only a small improvement of 3% is found for the use of Au NPs with respect to the pure $MAPbBr_3$-SCN, but a rather strong improvement of 20% is found for the NRs. The PLQY values of the materials were also determined and exhibit

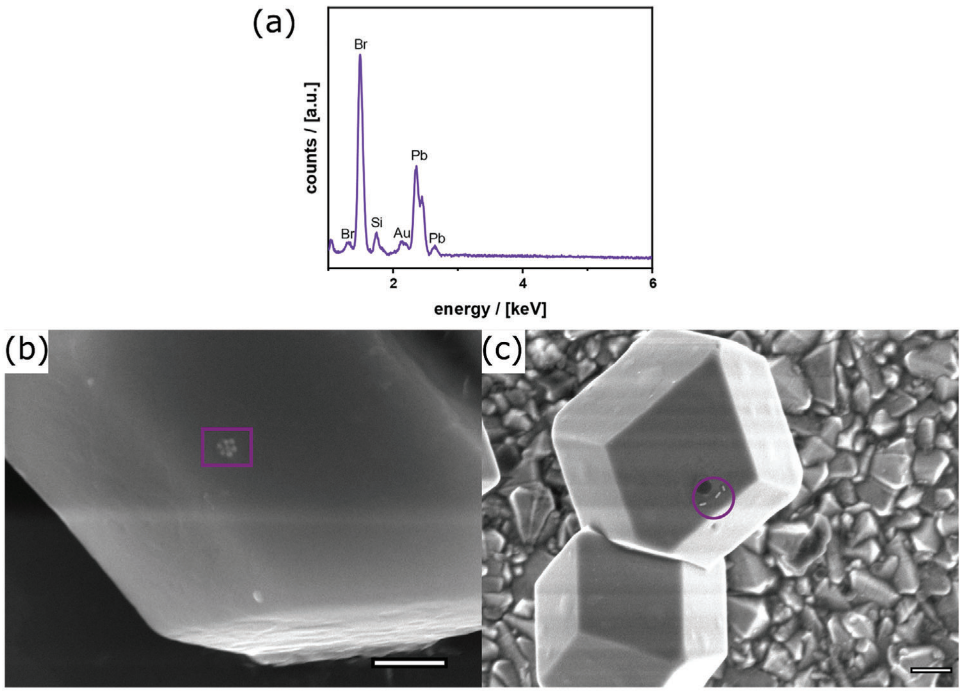

Figure 7. a) EDX spectrum of Au NP binary system revealing the presence of Au; b) SEM image of Au NPs (purple square) and c) Au NRs (purple circle) on the surface of $MAPbBr_3$-SCN microcrystals; scalebars = 250 nm.

the same trend (Figure S31a, Supporting Information). A possible explanation for the enhanced lifetime and emission is the increased outcoupling due to the randomly distributed Au NRs on the perovskite surface, acting as waveguides for the emitted light. This effect has been previously reported, for other semiconductor materials functionalized with Ag nanoparticles, which provide a strong scattering effect and thus increase the number of surface states.[66] To determine and understand the underlying physical mechanisms of the reported enhancement, ultrafast spectroscopic investigations will be required. In particular, the binary system of NRs, due to their anisotropy, offers great potential to gain insight through a possible excitation or emission of larger wavelengths, not affecting the excitation of the perovskite itself, probing whether there is an energetic exchange, or not.[64]

3. Conclusion

In this work a one-step aerosol-assisted ITC approach for SCN-passivated SC $MAPbBr_3$ microcrystals is presented. The crystallization kinetics, i.e., how the crystallization process and thus the morphology is affected by different (pseudo-)halide additives, was visualized by time-dependent UV–vis measurements. These investigations show that an increasing amount accelerates the crystallization as it has already been demonstrated for increasing MABr ratios.[38] Furthermore, the results show that not only

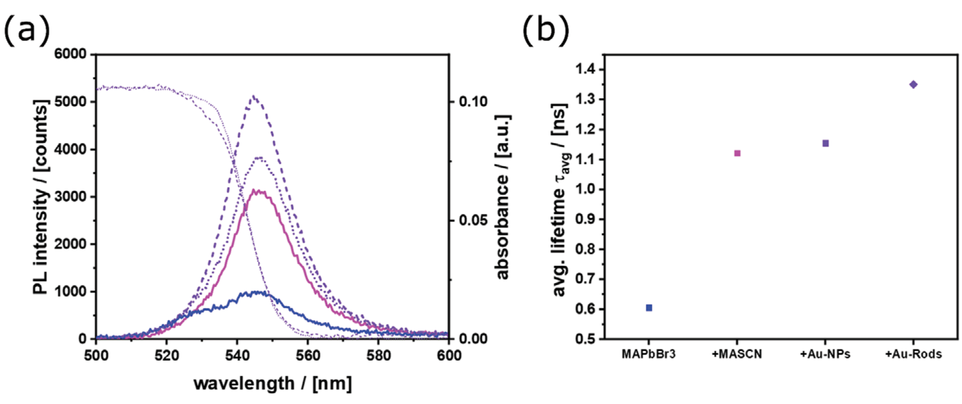

Figure 8. a) PL spectra of $MAPbBr_3$ (blue), $MAPbBr_3$-MASCN (magenta) and $MAPbBr_3$-SCN binary system with spherical Au NPs (purple, dotted) and nanorods (purple, dashed) and corresponding UV–vis absorbance spectra (lighter purple); and b) PL lifetimes determined via mono-exponential fit from PL decay spectra for $MAPbBr_3$ reference, $MAPbBr_3$-SCN and binary systems.

the amount but also the anionic species itself has an effect on the activity of the lead species and thus on the preferred formation of different crystal facets, i.e., the morphology of the crystals formed. The addition of MASCN does not suppress the SC formation, but results in a passivation layer that increases the stability of the SC $MAPbBr_3$ microcrystals against humidity. This increase in stability is directly attributed to the chemical modification of the surface and does not depend on any size-dependent or structural changes, as has been reported for polycrystalline materials and nanoparticles of different compositions.[40,54,55] In addition, the optoelectronic properties of the final $MAPbBr_3$-SCN microcrystals are superior compared to the $MAPbBr_3$ reference, showing longer charge carrier lifetimes and reduced SPV. This improvement is explained by the surface passivation resulting in the reduction of surface defect states. Therefore, by transferring the synthetic approach reported to the preparation of macroscopic SCs, their properties and stability is expected to be further improved without the need for multiple synthetic steps.[23] Finally, due to their enhanced stability the SCN-passivated microcrystals could be used to be combined with plasmonic Au nanostructures via an aerosol-assisted approach. First results regarding the optical properties show an enhancement of the charge carrier lifetimes and the PL emission. A possible explanation is that the Au nanostructures act as waveguides for the emitted radiation. To further determine whether additional charge carrier or energy transfer effects play a role, further investigations using ultrafast spectroscopic methods will be required. To clarify these considerations, the binary model system offers great potential for further investigations of these fundamental processes, and the presented aerosol approach offers a simple approach for their preparation.

4. Experimental Section

Chemicals: Extra dry N.N-dimethylformamide (99.8%) was purchased from Fisher Scientific and used as received. $PbBr_2$, methylammonium chloride (MACl), triethyleneglycol (TEG), HBr, and methylammonium solutions were purchased from Merck and used without further purification. MASCN was purchased from greatcellsolar materials and used as received. MABr was prepared according to an established synthesis.[3] Au NPs and nanorods dispersion were purchased from Merck and used as received. Two different dispersion were used for this work, a 10 nm spherical Au NP containing, phosphate-buffered saline (PBS) stabilized dispersion and a 10 nm diameter nanorods dispersion stabilized with Cetyltrimethylammoniumbromide (CTAB).

SSP Synthesis and Aerosol Process: All syntheses were carried out under inert gas atmosphere. All solid chemicals were dried under vacuum at 65 °C for at least 24 h before used. The precursor synthesis as reported earlier was adapted for this work. In a typical precursor synthesis, a 0.3 м solution of $PbBr_2$ in TEG was prepared. The solution was degassed at 65 °C under vacuum and stirring for 20 h and cooled to room temperature. To receive the liquid SSP, a second 0.3 м $PbBr_2$ and 0.6 м MABr solution in DMF was prepared. Finally, the two solutions were combined by a 1:1 (v:v) ratio. To obtain SSPs with an excess of different MA salts (MAI, MABr, MACl, and MASCN), the corresponding amount has been added to the DMF solution. The aerosol process and setup for the perovskite micro-crystal synthesis was the same as reported in our previous works.[38,39] A reservoir vessel was equipped with the aerosol generator (model 3076, TSI Inc.) to create the aerosol from the liquid SSP. This aerosol was transferred through a tubular oven (diameter 2.6 cm, length 50 cm) heated to 150 °C using a nitrogen flow of 2 l min^{-1}. The microcrystals were collected on different substrates (Si wafer, glass, or FTO-slides) without further treatment. Prior to particle collection the substrates were oxygen plasma cleaned (Femto plasma cleaner, Diener electronic GmbH). In a typical aerosol conversion 5 ml of the corresponding SSP were used, resulting in a reaction time of 90 min.

For the preparation of the binary gold-perovskite system, the original aerosol setup was modified, by using a shorter tubular oven with a length of 25 cm instead of 50 cm. For creation of the aerosol, the aerosol generator mentioned above was used. To combine Au nanoparticles and hybrid perovskite crystals, the substrates with hybrid perovskite micro-crystals were placed behind the oven and the Au nanoparticles were immobilized on the surface. The synthesis of the binary system was carried out with materials on appropriate substrates for the different analytical methods applied, as reported earlier.[38,39]

Stability Tests: A relative humidity of 53% has been achieved by using the delisquescene of $Ca(NO_3)_2$*$4H_2O$ at room temperature. Therefore, a supersaturated solution of the salt was placed in a closed glass bottle, to create the defined atmosphere. To prevent the materials from degradation caused by other triggers, the glass bottles were stored under strict exclusion of other influence, e.g. the exclusion of light. To investigate the influence of irradiation, a LED (630 nm) setup with an overall power of 100 W was used (7 V, 5.6 A). The wavelength of 630 nm was used, to make sure, the irradiation could not cause any excitation over bandgap energy of the material. Additionally, for the irradiation experiments, the samples were kept under inert gas atmosphere, and a slightly reduced pressure of 850 mbar was applied.

Analytical Methods: Scanning electron microscopy (SEM) images were performed using a Regulus 8230 from Hitachi. Energy dispersive X-ray (EDX) maps and spectra were measured with an EDX Oxford Ultim Max 100mm^2 windowless EDX detector. Transmission electron microscopy (TEM) images and electron diffraction (ED) pattern were obtained from a Hitachi HT7800 (120 kV) microscope. The carbon-coated copper grid was gently wiped over the sample deposited by the aerosol method. Mild illumination settings (condenser aperture of 50 µm and spot number 1 in F-Zoom mode) were used in order to produce a semi parallel beam of 1 µm in diameter (0.115 e^- $Å^{-2}$ s^{-1}). The 3D ED data were collected in continuous rotation mode with nano beam electron diffraction settings and crystal tracking.[67] Electron diffraction patterns were recorded (1 second per frame) with a CMOS camera (14 bit 5120 × 3840 pixels emsis Xarosa) at hardware-binning of 2 and acquired using the authors' own developed python program eHermelin[68] using SerialEM[69] as communication interface for the TEM. The crystals were continuously tilted in a maximum range of 100° with an angular speed of 1.009° s^{-1}. A total of 3 data sets from 3 crystals were recorded. PETS2.0 were used for 3D electron diffraction data processing. The structure was solved with Superflip[70] and refined with JANA.[71]

Powder diffraction was performed on a STOE transmission powder diffraction system (STADI P) in Debye-Scherrer geometry equipped with a Ge(111) monochromator (Cu-Kα_1 radiation, λ = 154.056 pm) and a MYTHEN 1K Stripdetector from DECTRIS. The measurement covered the range from 10° to 61° in 2θ with a step width of 0.015°. The software WinXPow, Version 2011 from Stoe & Cie was used for data acquisition. The samples were prepared, transferring the microcrystals from the Si-Wafers to the sample holders, using a small piece of Tesa strip. The measurements were carried out under standard conditions. A measurement of the pure Tesa strip was performed and used as reference to subtract from the sample measurements.

Samples were Au sputtered using a 108 Auto Sputter Coater from Cressington. For UV–vis spectra a Cary4000 from Agilent, equipped with a diffuse reflectance accessory was used. The temperature dependent UV–vis kinetic studies were performed using the same spectrometer but equipped with a Praying Mantis diffuse reflectance accessory from Agilent Technologies. To control the temperature of the sample, a heater with a WATLOW series 999 control unit from Harrick Scientific Products was used. FT-IR spectra were measured in reflectance using a Bruker IFS88 IR Microscope II, cooled with liquid nitrogen. Qualitative PL spectra were obtained from a UV–vis NIR spectrometer FLS 1000 from Edinburgh, using an excitation wavelength of 400 nm. PL-QY and lifetimes were determined using a FluoTime 300 from PicoQuant, equipped with a diffuse reflectance accessory, with an excitation wavelength of 405 nm. To obtain correct and reliable results for, 4 measurements of each sample at different points of the substrates were performed, following previous reports to eliminate statistical inconsistency of the samples for PL-QY.[72,73] Furthermore, an empty measurement was used as a reference for every single sample, where the substrate was rotated out of the beam, to eliminate the absorbance of diffuse scattered light by the substrate itself for each different sample. Due to laser inconsistency, only the first and last measurement of each sample were not considered. Kelvin Probe Force Microscopy (KPFM) measurements were conducted on an Oxford Instruments/Asylum Research MFP-3D Infinity AFM within a nitrogen glovebox (humidity level below 0.3%, oxygen level below 0.1%) for all experiments. The conductive cantilevers with Pt/Ir coating (Bruker Model: SCM-PIT-V2) had a typical resonance frequency of ≈75 kHz, a spring constant of 2 N m^{-1}, a tip radius of 25 nm, and a tip height ranging from 10 to 15 µm. Topography feedback was performed using amplitude modulation (AM) on the first eigenmode, and the oscillation amplitude was maintained at ≈20–30 nm for all measurements. Heterodyne KPFM experiments utilized a Zurich Instruments HF2 Lock-In Amplifier for KPFM feedback.[74,75] The electric drive amplitude of the ω_E signal varied between 2 and 5 V based on the signal obtained from the sample. The sample was grounded through the sample holder with an external wire connected to the ground level of the Zurich Lock-In Amplifier. The compensating V_{DC} was applied to the tip to minimize electrostatic tip–sample interactions. For surface photovoltage (SPV) measurements, the sample was illuminated from below by a pulsed laser (Cobolt 06-01 Series) at 488 nm. Laser power was controlled by custom-written code within the MFP3D's control software by the AFM controller (Asylum Research ARC2), which provided analog voltage to activate the illumination. Surface photovoltage values were obtained by extracting the dark surface potential from the light surface potential.

Supporting Information

Supporting Information is available from the Wiley Online Library or from the author.

Acknowledgements

This research was funded by the German Research Foundation (DFG), SPP2196 (Perovskite semiconductors: From fundamental properties to devices). The authors acknowledge the use of the equipment and the expert support usage and data analysis provided by cfMATCH. The authors thank C. Rüscher (department of mineralogy, Leibniz University Hannover) for providing access and introduction to the IR microscope.

Open access funding enabled and organized by Projekt DEAL.

Conflict of Interest

The authors declare no conflict of interest.

Data Availability Statement

The data that support the findings of this study are available in the supplementary material of this article.

Keywords

Au nanoparticles, crystallization kinetics, hybrid perovskite microcrystals, one-step synthesis, surface passivation

Received: June 13, 2024
Revised: August 1, 2024
Published online: September 2, 2024

[1] D. Weber, *Zeitschrift für Naturforschung B.* **1978**, *33*, 1443.
[2] D. B. Mitzi, in *Progress in Inorganic Chemistry*, Wiley, Hoboken, New Jersey **1999**, pp. 1–121.
[3] S. D. Stranks, G. E. Eperon, G. Grancini, C. Menelaou, M. J. P. Alcocer, T. Leijtens, L. M. Herz, A. Petrozza, H. J. Snaith, *Science* **2013**, *342*, 341.
[4] Q. Dong, Y. Fang, Y. Shao, P. Mulligan, J. Qiu, L. Cao, J. Huang, *Science* **2015**, *347*, 967.
[5] J. S. Manser, J. A. Christians, P. V. Kamat, *Chem. Rev.* **2016**, *116*, 12956.
[6] L. Schmidt-Mende, V. Dyakonov, S. Olthof, F. Ünlü, K. M. T. Lê, S. Mathur, A. D. Karabanov, D. C. Lupascu, L. M. Herz, A. Hinderhofer, F. Schreiber, A. Chernikov, D. A. Egger, O. Shargaieva, C. Cocchi, E. Unger, M. Saliba, M. M. Byranvand, M. Kroll, F. Nehm, K. Leo, A. Redinger, J. Höcker, T. Kirchartz, J. Warby, E. Gutierrez-Partida, D. Neher, M. Stolterfoht, U. Würfel, M. Unmüssig, et al., *APL Mater.* **2021**, *9*, 109202.
[7] X. He, Y. Deng, D. Ouyang, N. Zhang, J. Wang, A. A. Murthy, I. Spanopoulos, S. M. Islam, Q. Tu, G. Xing, Y. Li, V. P. Dravid, T. Zhai, *Chem. Rev.* **2023**, *123*, 1207.
[8] A. Fakharuddin, M. K. Gangishetty, M. Abdi-Jalebi, S.-H. Chin, A. R. bin Mohd Yusoff, D. N. Congreve, W. Tress, F. Deschler, M. Vasilopoulou, H. J. Bolink, *Nat. Electron.* **2022**, *5*, 203.
[9] H. Zhu, L. Pan, F. T. Eickemeyer, M. A. Hope, O. Ouellette, A. Q. M. Alanazi, J. Gao, T. P. Baumeler, X. Li, S. Wang, S. M. Zakeeruddin, Y. Liu, L. Emsley, M. Grätzel, *ACS Energy Lett.* **2022**, *7*, 1112.
[10] R. Kumar, P. Srivastava, T. Kumar, M. Bag, *J. Phys. Chem. C.* **2022**, *126*, 14305.
[11] N. Aristidou, I. Sanchez-Molina, T. Chotchuangchutchaval, M. Brown, L. Martinez, T. Rath, S. A. Haque, *Angew. Chem., Int. Ed.* **2015**, *54*, 8208.
[12] A. M. Askar, G. M. Bernard, B. Wiltshire, K. Shankar, V. K. Michaelis, *J. Phys. Chem. C.* **2017**, *121*, 1013.
[13] J. Schlipf, L. Bießmann, L. Oesinghaus, E. Berger, E. Metwalli, J. A. Lercher, L. Porcar, P. Müller-Buschbaum, *J. Phys. Chem. Lett.* **2018**, *9*, 2015.
[14] S. Premkumar, K. Kundu, S. Umapathy, *Nanoscale* **2019**, *11*, 10292.
[15] D. Shi, V. Adinolfi, R. Comin, M. Yuan, E. Alarousu, A. Buin, Y. Chen, S. Hoogland, A. Rothenberger, K. Katsiev, Y. Losovyj, X. Zhang, P. A. Dowben, O. F. Mohammed, E. H. Sargent, O. M. Bakr, *Science* **2015**, *347*, 519.
[16] X. Zheng, Y. Hou, H. T. Sun, O. F. Mohammed, E. H. Sargent, O. M. Bakr, *J. Phys. Chem. Lett.* **2019**, *10*, 2629.
[17] B. Murali, H. K. Kolli, J. Yin, R. Ketavath, O. M. Bakr, O. F. Mohammed, *ACS Mater. Lett.* **2020**, *2*, 184.
[18] B. Murali, E. Yengel, C. Yang, W. Peng, E. Alarousu, O. M. Bakr, O. F. Mohammed, *ACS Energy Lett.* **2017**, *2*, 846.
[19] Y. Almadori, D. Moerman, J. L. Martinez, P. Leclère, B. Grévin, *Beilstein J. Nanotechnol.* **2018**, *9*, 1695.
[20] W. Zhang, S. Pathak, N. Sakai, T. Stergiopoulos, P. K. Nayak, N. K. Noel, A. A. Haghighirad, V. M. Burlakov, D. W. deQuilettes, A. Sadhanala, W. Li, L. Wang, D. S. Ginger, R. H. Friend, H. J. Snaith, *Nat. Commun.* **2015**, *6*, 10030.
[21] V. Donchev, D. Regaldo, S. Georgiev, A. Bojar, M. da Lisca, K. Kirilov, J. Alvarez, P. Schulz, J.-P. Kleider, *ACS Omega* **2023**, *8*, 8125.
[22] L. Barnea-Nehoshtan, S. Kirmayer, E. Edri, G. Hodes, D. Cahen, *J. Phys. Chem. Lett.* **2014**, *5*, 2408.
[23] L. Chen, H. Wang, W. Zhang, F. Li, Z. Wang, X. Wang, Y. Shao, J. Shao, *ACS Appl. Mater. Interfaces* **2022**, *14*, 10917.
[24] X. Guo, N. Li, Y. Xu, J. Zhao, F. Cui, Y. Chen, X. Du, Q. Song, G. Zhang, X. Cheng, X. Tao, Z. Chen, *Adv. Funct. Mater.* **2023**, *33*, 2213995.

[25] J. Xia, C. Liang, H. Gu, S. Mei, S. Li, N. Zhang, S. Chen, Y. Cai, G. Xing, *Energy Environ. Mater.* **2023**, *6*, e12296.
[26] P.-Y. Lin, A. Loganathan, I. Raifuku, M.-H. Li, Y.-Y. Chiu, S.-T. Chang, A. Fakharuddin, C.-F. Lin, T.-F. Guo, L. Schmidt-Mende, P. Chen, *Adv. Energy Mater.* **2021**, *11*, 2100818.
[27] S. Wang, C. Wu, H. Yao, L. Ding, F. Hao, *Mater. Chem. Front.* **2023**, *7*, 789.
[28] A. Hossain, P. Bandyopadhyay, A. Karmakar, A. K. M. A. Ullah, R. K. Manavalan, K. Sakthipandi, N. Alhokbany, S. M. Alshehri, J. Ahmed, *Ceram. Int.* **2022**, *48*, 7325.
[29] A. Soultati, M. Tountas, K. K. Armadorou, A. R. bin Mohd Yusoff, M. Vasilopoulou, M. Khaja Nazeeruddin, *Energy Adv.* **2023**, *2*, 1075.
[30] M. I. Saidaminov, A. L. Abdelhady, B. Murali, E. Alarousu, V. M. Burlakov, W. Peng, I. Dursun, L. Wang, Y. He, G. Maculan, A. Goriely, T. Wu, O. F. Mohammed, O. M. Bakr, *Nat. Commun.* **2015**, *6*, 7586.
[31] M. I. Saidaminov, A. L. Abdelhady, G. Maculan, O. M. Bakr, *Chem. Commun.* **2015**, *51*, 17658.
[32] T. Kollek, D. Gruber, J. Gehring, E. Zimmermann, L. Schmidt-Mende, S. Polarz, *Angew. Chem.-Int. Ed.* **2015**, *54*, 1341.
[33] T. Kollek, C. Fischer, I. Gottker-Schnetmann, S. Polarz, *Chem. Mat.* **2016**, *28*, 4134.
[34] T. Kollek, D. Wurmbrand, S. T. Birkhold, E. Zimmermann, J. Kalb, L. Schmidt-Mende, S. Polarz, *ACS Appl. Mater. Interfaces* **2017**, *9*, 1077.
[35] N. Fillafer, T. Seewald, L. Schmidt-Mende, S. Polarz, *Beilstein J. Nanotechnol.* **2020**, *11*, 466.
[36] N. Fillafer, H. Kuper, A. Schaate, S. Locmelis, J. A. Becker, Y. Krysiak, S. Polarz, *Adv. Funct. Mater.* **2022**, *32*, 2201126.
[37] T. Kollek, S. Polarz, *CrystEngComm* **2017**, *19*, 4615.
[38] U. J. Bahnmüller, H. Kuper, T. Seewald, Y. Yalçinkaya, J. A. Becker, L. Schmidt-Mende, S. A. L. Weber, S. Polarz, *Nanomaterials* **2021**, *11*, 3057.
[39] U. J. Bahnmüller, Y. Krysiak, S. Locmelis, S. Polarz, *Cryst. Growth Des.* **2022**, *22*, 4948.
[40] M. Kyung Kim, T. Jeon, H. Il Park, J. Min Lee, S. Ah Nam, S. Ouk Kim, *CrystEngComm* **2016**, *18*, 6090.
[41] D. Di, K. P. Musselman, G. Li, A. Sadhanala, Y. Ievskaya, Q. Song, Z.-K. Tan, M. L. Lai, J. L. MacManus-Driscoll, N. C. Greenham, R. H. Friend, *J. Phys. Chem. Lett.* **2015**, *6*, 446.
[42] J. A. Sichert, Y. Tong, N. Mutz, M. Vollmer, S. Fischer, K. Z. Milowska, R. García Cortadella, B. Nickel, C. Cardenas-Daw, J. K. Stolarczyk, A. S. Urban, J. Feldmann, *Nano Lett.* **2015**, *15*, 6521.
[43] S. Carretero-Palacios, M. E. Calvo, H. Míguez, *J. Phys. Chem. C.* **2015**, *119*, 18635.
[44] W. Zhang, M. Saliba, S. D. Stranks, Y. Sun, X. Shi, U. Wiesner, H. J. Snaith, *Nano Lett.* **2013**, *13*, 4505.
[45] M. Saliba, W. Zhang, V. M. Burlakov, S. D. Stranks, Y. Sun, J. M. Ball, M. B. Johnston, A. Goriely, U. Wiesner, H. J. Snaith, *Adv. Funct. Mater.* **2015**, *25*, 5038.
[46] X. Cao, L. Zhi, Y. Li, F. Fang, X. Cui, L. Ci, K. Ding, J. Wei, *ACS Appl. Energy Mater.* **2018**, *1*, 868.
[47] J. Hieulle, X. Wang, C. Stecker, D.-Y. Son, L. Qiu, R. Ohmann, L. K. Ono, A. Mugarza, Y. Yan, Y. Qi, *J. Am. Chem. Soc.* **2019**, *141*, 3515.
[48] D. M. Jang, K. Park, D. H. Kim, J. Park, F. Shojaei, H. S. Kang, J.-P. Ahn, J. W. Lee, J. K. Song, *Nano Lett.* **2015**, *15*, 5191.
[49] V. Diez-Cabanes, J. Even, D. Beljonne, C. Quarti, *Adv. Opt. Mater.* **2021**, *9*, 2001832.
[50] A. Jaffe, Y. Lin, C. M. Beavers, J. Voss, W. L. Mao, H. I. Karunadasa, *ACS Cent. Sci.* **2016**, *2*, 201.
[51] B. Brunetti, C. Cavallo, A. Ciccioli, G. Gigli, A. Latini, *Sci. Rep.* **2016**, *6*, 31896.
[52] *Lange's Handbook of Chemistry*, (Eds.: J. A. Dean, N. A. Lange), McGraw-Hill, New York **1985**.
[53] L. Yang, J. Wang, W. W.-F. Leung, *ACS Appl. Mater. Interfaces* **2015**, *7*, 14614.
[54] W. Ke, C. Xiao, C. Wang, B. Saparov, H.-S. Duan, D. Zhao, Z. Xiao, P. Schulz, S. P. Harvey, W. Liao, W. Meng, Y. Yu, A. J. Cimaroli, C.-S. Jiang, K. Zhu, M. Al-Jassim, G. Fang, D. B. Mitzi, Y. Yan, *Adv. Mater.* **2016**, *28*, 5214.
[55] T. Cai, F. Li, Y. Jiang, X. Liu, X. Xia, X. Wang, J. Peng, L. Wang, W. A. Daoud, *Nanoscale* **2019**, *11*, 1319.
[56] A. Mahapatra, N. Parikh, H. Kumari, M. K. Pandey, M. Kumar, D. Prochowicz, A. Kalam, M. M. Tavakoli, P. Yadav, *J. Appl. Phys.* **2020**, *127*, 185501.
[57] H. Kim, Y. Ho Lee, T. Lyu, J. Heun Yoo, T. Park, J. Hak Oh, *J. Mater. Chem. A.* **2018**, *6*, 18173.
[58] Z. Q. Tian, B. Ren, B. W. Mao, *J. Phys. Chem. B.* **1997**, *101*, 1338.
[59] Z. Wang, T. Liu, X. Long, Y. Li, F. Bai, S. Yang, *J. Phys. Chem. C.* **2019**, *123*, 9282.
[60] Q. Jiang, D. Rebollar, J. Gong, E. L. Piacentino, C. Zheng, T. Xu, *Angew. Chem., Int. Ed.* **2015**, *54*, 7617.
[61] S. Venkatesan, E. Ngo, D. Khatiwada, C. Zhang, Q. Qiao, *ACS Appl. Mater. Interfaces* **2015**, *7*, 16093.
[62] J. H. Kim, J. Lee, J. H. Kim, C. C. Hwang, C. Lee, J. Y. Park, *Appl. Phys. Lett.* **2015**, *106*, 251606.
[63] T. S. Sherkar, C. Momblona, L. Gil-Escrig, J. Avila, M. Sessolo, H. J. Bolink, L. J. A. Koster, *ACS Energy Lett.* **2017**, *2*, 1214.
[64] Y. Xia, N. J. Halas, *MRS Bull.* **2005**, *30*, 338.
[65] C. Yang, C. P. Wong, M. M. F. Yuen, *J. Mater. Chem. C.* **2013**, *1*, 4052.
[66] H.-J. Song, J. Han, G. Lee, J. Sohn, Y. Kwon, M. Choi, C. Lee, *Org. Electron.* **2018**, *52*, 230.
[67] S. Plana-Ruiz, Y. Krysiak, J. Portillo, E. Alig, S. Estradé, F. Peiró, U. Kolb, *Ultramicroscopy* **2020**, *211*, 112951.
[68] Y. Schmidt, *Analyse von Diffusionspfaden in Lithium-Festkörßerelektrolyten Mittels 3D-Elektronenbeugung*, Leibniz University Hannover, Hannover **2023**.
[69] D. N. Mastronarde, *Microsc. Microanal.* **2018**, *24*, 864.
[70] L. Palatinus, G. Chapuis, *J. Appl. Cryst.* **2007**, *40*, 786.
[71] V. Petříček, L. Palatinus, J. Plášil, M. Dušek, *Z. Kristallogr. Cryst. Mater.* **2023**, *238*, 271.
[72] J. C. de Mello, H. F. Wittmann, R. H. Friend, *Adv. Mater.* **1997**, *9*, 230.
[73] F. Fries, S. Reineke, *Sci. Rep.* **2019**, *9*, 15638.
[74] J. L. Garrett, J. N. Munday, *Nanotechnology* **2016**, *27*, 245705.
[75] A. Axt, I. M. Hermes, V. W. Bergmann, N. Tausendpfund, S. A. L. Weber, *Beilstein J. Nanotechnol.* **2018**, *9*, 1809.

